

Schwarzschild Black Hole Surrounded by Perfect Fluid Dark Matter in the presence of Quintessence Matter Field

B. Hamil*

Orcid ID : 0000-0002-7043-6104,

Laboratoire de Physique Mathématique et Subatomique,
Faculté des Sciences Exactes, Université Constantine 1, Constantine, Algeria.

B. C. Lütfüoğlu†

Orcid ID : 0000-0001-6467-5005,

Department of Physics, University of Hradec Králové,
Rokitanského 62, 500 03 Hradec Králové, Czechia.

April 11, 2024

Abstract

In this manuscript, we examine the Schwarzschild black hole surrounded by perfect fluid dark matter in the presence of the quintessence matter field in the context of thermodynamics, shadows, and quasinormal modes. We find that the quintessence matter field sets an upper bound value on the horizon where dark matter settles a lower limit on the event horizon but also expands the upper bound value of the horizon. We discuss how this impact alters the black hole's thermodynamics, shadows, and quasinormal modes.

1 Introduction

The universe is a great, mysterious puzzle. Just when we believe we have the clue to solve a piece of this puzzle, we are confronted with the reality of how little we understand. At the very beginning of this century, we thought that with the observation of the Higgs boson, the Standard Model would be roughly complete, and hence, we would be able to explain important phenomena. After the discovery of the Higgs boson, we obtained reliable clues that reveal that only about 5% of our universe is composed of directly observable ordinary matter, and the rest is a combination of dark matter and dark energy [1, 2]. So far we have not directly observed these dark sector components, but through indirect findings, we have been able to discuss evidence of their existence [3, 4]. For example, in the literature, the presence of dark matter was predicted by the rotation curves of spiral galaxies [5–7], dynamical stability of disk galaxies [8, 9], large-scale structure formation of the universe [10], gravitational lensing observations by galaxies and clusters of galaxies [11, 12], cosmic microwave background [13, 14], and baryon acoustic oscillations [15]. Many theories have been put forward so far to model dark matter [16–21]. Most of these theories go beyond the Standard Model [22–29], while few of them do not [30–33]. Among all

*hamilbilel@gmail.com

†bekir.lutfuoglu@uhk.cz (Corresponding author)

these models, the perfect fluid dark matter (PFDM) model, which treats dark matter as a perfect fluid, presents interesting theoretical aspects. For example, Kiselev derived exact static spherically symmetric black hole solutions out of Einstein equations with the PFDM [34]. Later, Li et al used the logarithmic term, which arises from the PFDM model of Kiselev, to discuss the asymptotic rotation curves for the dark matter in the halo-dominated region [35]. In another work, Xu et al generalized Kiselev's solution to Kerr-like black holes employing the Newman-Janis method and examined Kerr-(A)dS black hole properties [36]. Soon after this work, PFDM impacts on deflection angle, black hole's shadow, naked singularity, and thermal properties were investigated in [37–40]. We observe that in very recent works the features of other black holes such as Reissner-Nordström, Reissner-Nordström-AdS, Schwarzschild, Schwarzschild-dS, and non-linear magnetic-charged AdS black holes were studied by assuming PFDM surrounded them [41–48].

Reliable astronomical observations put forward that our universe is expanding at an accelerating rate [49–51], and dark energy, the other component of the dark sector, is thought to be behind this fact. The cosmological constant, whose observational and theoretical values differ by 120 orders of magnitude [52], cannot explain this expansion. Theoretical physicists proposed new models using dynamical scalar fields to describe dark energy, taking into account that the cosmological constant does not alter with time [53–60]. Among different models, the quintessence matter model stands in the form where the equation of state is limited by the linear relationship between pressure, energy density and a state parameter [55]. Using the quintessence matter field, Kiselev solved Einstein's equation and obtained a general solution form of the static spherically symmetric black hole [61]. Subsequently, in the presence of quintessence matter new solutions of other black holes were obtained, and the impacts of the quintessence field on their thermal quantities, shadows, and quasinormal modes were discussed widely in [62–89].

Although black hole solutions have been sought for more than a century, the problem of their detection remained an open debate. Until the successful observational results of the Event Horizon Telescope were published [90–94], some authors suggested that not the black holes but their shadows could be detected [95–97]. According to this proposal, if a black hole is located between a light source and an observer, it should be expected that some of the light rays would be deflected by the intense gravitational field of the black hole and reach the observer. However, some photons would fall into the black hole instead of this deflection and create a dark region called a shadow. The apparent shape of the black hole is assumed to correspond to the boundary of the shadow. Nowadays, we observe many papers that examine the impact the space-time geometry, dark energy, and dark matter on shadow images in the literature [98–133].

On the other hand, the detection of gravitational waves has provided new clues to solve our puzzle [134, 135]. Advanced observations of gravitational waves in particular can be employed to test many alternative theories of general relativity. Black holes, which are in their final stage, are assumed to emit gravitational waves in the form of quasinormal radiation [136]. Mathematically, quasinormal modes are considered to be in complex number forms, where the real and imaginary sections are associated with the actual oscillation and the inverse damping time, respectively [137]. Since they are independent of the initial perturbation, they are frequently assumed as the fingerprints of black holes [138]. In literature, numerous studies have been conducted by using analytic and numerical methods to delve into quasinormal modes of black holes within various scenarios [139–167].

In this contribution, we intend to explore thermodynamics, shadows, and quasinormal modes features of Schwarzschild black hole surrounded by PFDM in the presence of the quintessence matter field. To achieve our goal we organize the paper as follows: In Sec. 2, we present a brief review of the mathematical construction of the considered scenario. Then, in Sec. 3, we delve into its thermodynamics. In Sec. 4, we describe the expected shadow images. After that, in Sec. 5, we derive the quasinormal modes by using two different approaches. Finally, we conclude the manuscript in Sect. 6. Here, we have to note that in the rest of the manuscript, we assume $G = c = \hbar = k_B = 1$.

2 Black Hole Solution

We begin with the action that describes the Schwarzschild black hole surrounded by PFDM [35,36,42]

$$\mathcal{S}_0 = \int d^4x \sqrt{-g} \left[\frac{1}{16\pi} (R - 2\Lambda) - 4\pi \mathcal{L}_{PFDM} \right]. \quad (1)$$

Here, g and R denote the determinant of the metric tensor and the scalar curvature, respectively. Then, we consider the quintessence matter field to model the impact of dark energy [168]

$$\mathcal{S} = \mathcal{S}_0 + \int d^4x \sqrt{-g} \mathcal{L}_q, \quad (2)$$

where the quintessence field Lagrange density is given in terms of the quintessential scalar field, ϕ , and the potential, $V(\phi)$, as [169]

$$\mathcal{L}_q = -\frac{1}{2} (\nabla\phi)^2 - V(\phi). \quad (3)$$

Following the least action principle, we obtain the field equation in the form of [170]

$$R_{\mu\nu} - \frac{1}{2} g_{\mu\nu} R + g_{\mu,\nu} \Lambda = -8\pi \left(\bar{T}_{\mu\nu} + T_{\mu\nu}(PFDM) - T_{\mu\nu}(q) \right). \quad (4)$$

Since we consider dark matter as a type of perfect fluid, we can formulate the energy-momentum tensor in terms of energy density and pressure as

$$T_{\mu}^{\nu} = [-\rho, p, p, p], \quad (5)$$

In the simplest scenario, the ratio of energy density to pressure is assumed to have a constant value, $\frac{\rho}{p} = \delta - 1$, [35]. The spherical symmetric solution of the field equations gives the Schwarzschild black hole solution in the form of [42,170]

$$ds^2 = -f(r) dt^2 + \frac{1}{f(r)} dr^2 + r^2 d\Omega^2, \quad (6)$$

with the lapse function, $f(r)$,

$$f(r) = 1 - \frac{2M}{r} - \frac{\sigma}{r^{3\omega_q+1}} + \frac{\alpha}{r} \ln \frac{r}{|\alpha|}. \quad (7)$$

Here, α is the PFDM intensity, and σ and ω_q are the normalization factor and the quintessence state parameters, respectively.

We notice that the quintessence state parameter, which varies between $-1/3 < \omega_q < -1$, has a crucial impact on the lapse function. Therefore we have to discuss black hole properties with specific values of it. To be consistent throughout the rest of the manuscript, we choose the following four values: $\omega_q = -0.35$, $\omega_q = -0.55$, $\omega_q = -0.75$, and $\omega_q = -0.95$. At first in Fig. 1 we depict the lapse function with these parameters versus radius.

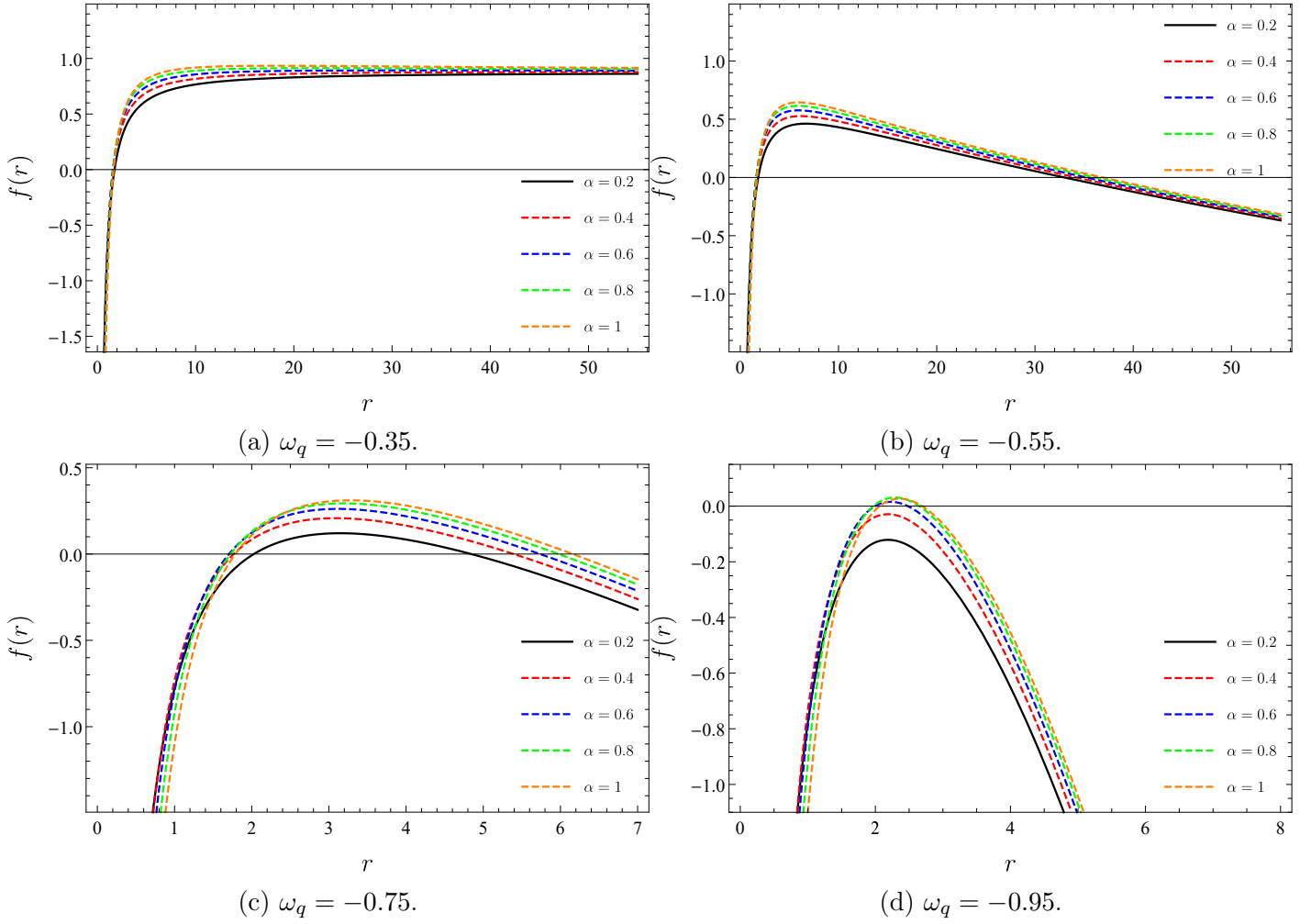


Figure 1: The impact of the dark matter and dark energy on the lapse function of Schwarzschild black hole for $\sigma = 0.1$ and $M = 1$.

We observe that the quintessence state parameter alters the concavity of the lapse function which is important in the context of the event horizon and naked singularity. For example, for $\omega_q = -0.35$ there is only one horizon. In this case, the dark matter parameter does not significantly influence the horizon radius. However, for smaller quintessence state parameters the concavity increases. For instance, for $\omega_q = -0.55$, we observe two horizons. Here, we note that for greater α values, the greater horizon radii take slightly greater values. For much smaller quintessence matter parameters, we see this impact more apparently. For example, for $\omega_q = -0.75$, the greater horizon radii occur relatively at smaller horizon values because of the larger concavity. All these cases are free of a naked singularity. However, for much smaller quintessence state parameters, for instance, for $\omega_q = -0.95$, the concavity increases so much that the lapse function may not reach zero for any radius. In this case, naked singularity can appear. On the other hand, with greater dark matter parameters an event horizon can occur and the naked singularity problem can be resolved. It is worth noting that these generic scenarios are plotted for a random mass value, $M = 1$. For a different mass value, it is possible that there is no naked singularity.

Next, we use the horizon equation

$$f(r) \Big|_{r=r_H} = 0, \quad (8)$$

for deriving the mass function in terms of the event horizon. We find

$$M = \frac{r_H}{2} - \frac{\sigma}{2r_H^{3\omega_q}} + \frac{\alpha}{2} \ln \frac{r_H}{|\alpha|}. \quad (9)$$

In Figure 2 we demonstrate how the mass function varies with the event horizon using the parameters employed above.

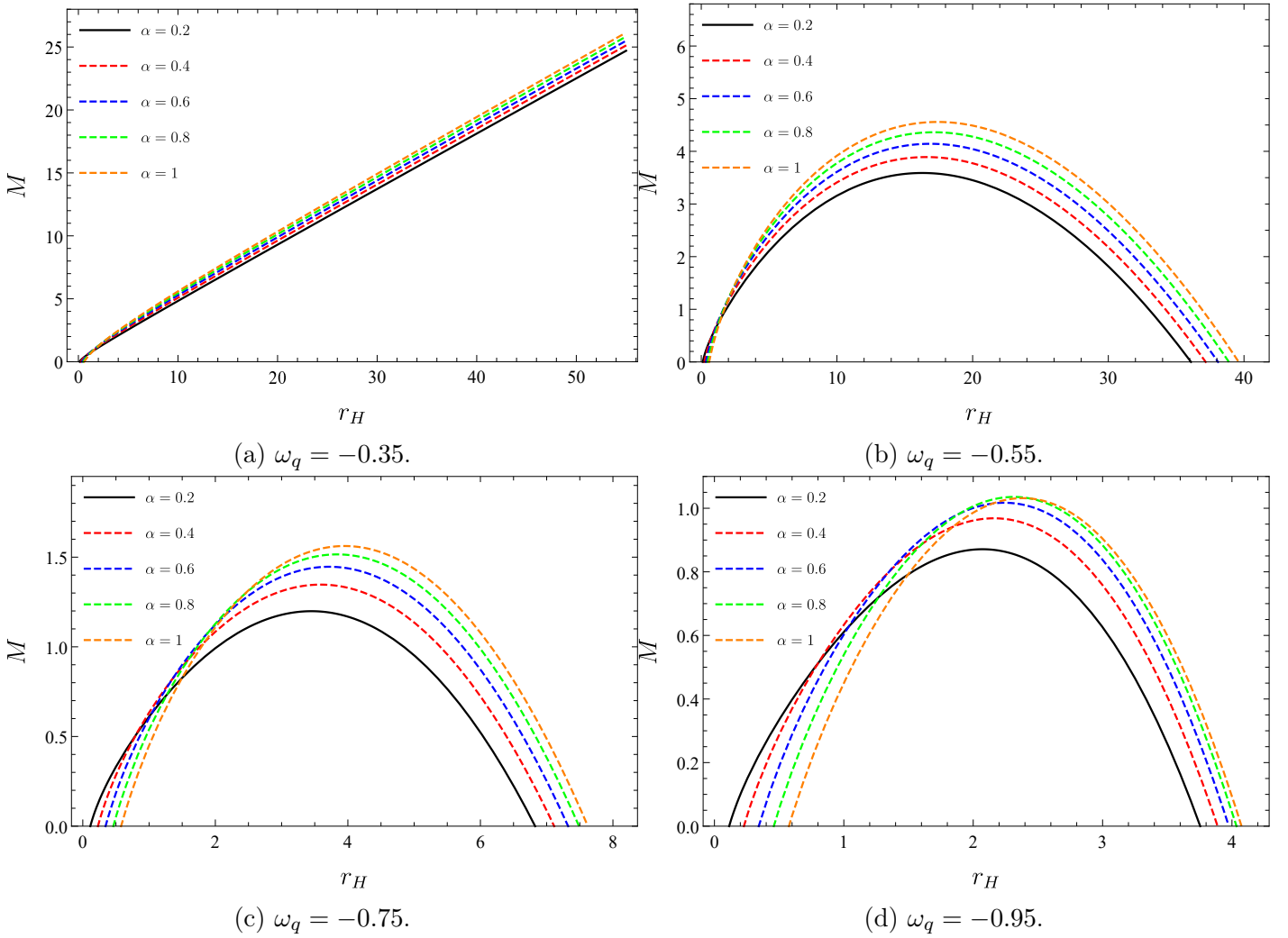


Figure 2: The impact of the dark matter and dark energy on the Schwarzschild black hole mass for $\sigma = 0.1$.

Fig. 2a shows that the mass function monotonously increases versus the event horizon. This finding is compatible with the presence of one event horizon. Here, we have to note that an increase in the dark matter parameter slightly affects the increase of the mass function. For smaller quintessence state parameters we observe that the monotonic increase of the mass function is no longer valid. In these cases, we observe that there is a lower limit as well as an upper limit on the event horizon. In Fig. 2b, where $\omega_q = -0.55$, we hardly can detect these lower limit values since the upper limit values are much more greater than them. However, for $\omega_q = -0.75$ and $\omega_q = -0.95$, these lower bounds and intervals become apparent. In both cases, we observe a shift in the gap length as the impact of the dark matter parameter variation. To be more precise, we numerically calculate the lower and upper bound event horizon radii for these scenarios and present them in Table 1.

α	$\omega_q = -0.35$		$\omega_q = -0.55$		$\omega_q = -0.75$		$\omega_q = -0.95$	
	$r_{H_{min}}$	$r_{H_{max}}$	$r_{H_{min}}$	$r_{H_{max}}$	$r_{H_{min}}$	$r_{H_{max}}$	$r_{H_{min}}$	$r_{H_{max}}$
0.2	0.117	∞	0.114	36.093	0.114	6.827	0.114	3.755
0.4	0.235	∞	0.230	37.177	0.228	7.114	0.227	3.890
0.6	0.352	∞	0.347	38.087	0.344	7.325	0.342	3.976
0.8	0.470	∞	0.464	38.888	0.460	7.489	0.458	4.035
1.0	0.588	∞	0.582	39.610	0.578	7.622	0.575	4.075

Table 1: The event horizon range that determines physical black hole mass with $\sigma = 0.1$.

We observe that for smaller quintessence state parameter values, the lower and upper bound horizon radii values take smaller values. We also notice that the dark matter parameter affects the maximum mass value of the black hole in such a way that for greater dark matter parameters, the black hole achieves its maximum mass value at a larger event horizon.

3 Black Hole's Thermodynamics

In this section, we will derive the important thermal functions of the black hole we are considering and discuss the impact of dark matter and dark energy on them. As usual, we start with the Hawking temperature which can be obtained in the semi-classical framework using the relationship between surface gravity and metric components [171]

$$T_H = \frac{\kappa}{2\pi} = \frac{1}{4\pi} \frac{d}{dr} f(r) \Big|_{r=r_H}. \quad (10)$$

Substituting Eqs. (7) and (9) in Eq. (10), we obtain a relation between the Hawking temperature and event horizon radius

$$T_H = \frac{1}{4\pi r_H} \left(1 + \frac{\alpha}{r_H} + \frac{3\sigma\omega_q}{r_H^{1+3\omega_q}} \right). \quad (11)$$

We observe that the Hawking temperature, which depends on the parameters of the dark energy and dark matter, reduces to the ordinary case for $\alpha = \sigma = 0$ [172]. Moreover, only in the absence of the quintessence field Eq. (11) turns to

$$T_H = \frac{1}{4\pi r_H} \left(1 + \frac{\alpha}{r_H} \right), \quad (12)$$

which has to be named as the Hawking temperature of the Schwarzschild black hole in the background of PFDM. Similarly, only in the absence of the dark matter Eq. (11) reduces to the Hawking temperature of Schwarzschild black hole surrounded by the dark energy in the form of [78]

$$T_H = \frac{1}{4\pi r_H} \left(1 + \frac{3\sigma\omega_q}{r_H^{1+3\omega_q}} \right). \quad (13)$$

Now, we examine the Hawking temperature within four cases as above. To this end, we plot Fig. 3 and illustrate the variation of Hawking temperatures with respect to the event horizon.

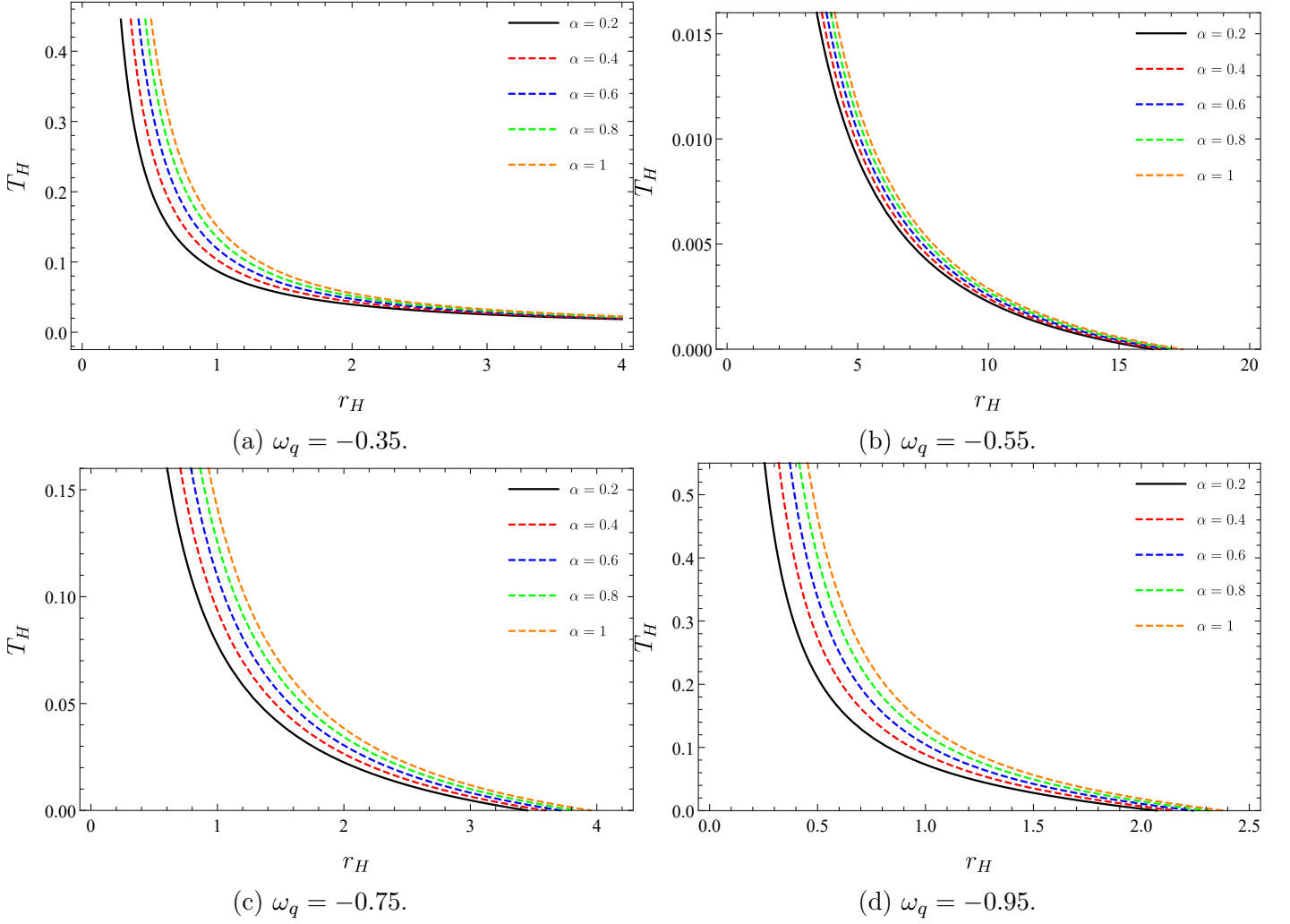


Figure 3: Behavior of the Hawking temperature in terms of event horizon for different values of α and $\sigma = 0.1$.

Fig. 3 shows that the Hawking temperature decreases in all cases as the event horizon increases similar to the ordinary case. However, only for $\omega_q = -0.35$, the Hawking temperature tends to zero at infinite horizon radius as in the standard case. For the other three cases, the Hawking temperature becomes zero at an upper bound horizon value and the PFDM parameter affects that value. In fact, we observe in all cases, for a fixed event horizon radius within a physically meaningful range, black holes with greater dark matter parameters would have higher temperatures.

Then, we explore the effect of the dark energy. To determine it, we depict Fig. 4 using two fixed values of the PFDM parameter.

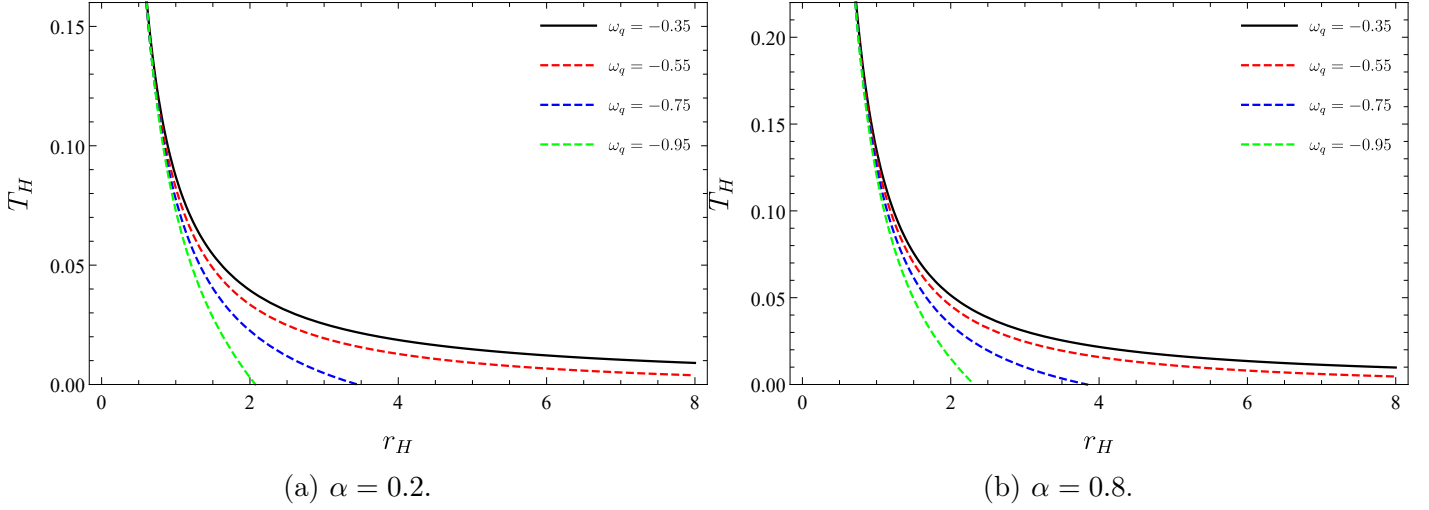


Figure 4: Behavior of the Hawking temperature in terms of event horizon for different values of ω_q and $\sigma = 0.1$.

We observe that for greater quintessence state parameters Hawking temperature decreases faster. Now, we use numerical methods to calculate the upper bound of the event horizon and the black hole mass values at those radii. We tabulate our results in Table 2.

α	$\omega_q = -0.35$		$\omega_q = -0.55$		$\omega_q = -0.75$		$\omega_q = -0.95$	
	r_H	M_H	r_H	M_H	r_H	M_H	r_H	M_H
0.2	∞	∞	16.294	3.589	3.450	1.199	2.072	0.871
0.4	∞	∞	16.578	3.891	3.589	1.347	2.160	0.968
0.6	∞	∞	16.874	4.143	3.717	1.447	2.240	1.017
0.8	∞	∞	17.152	4.362	3.838	1.515	2.314	1.036
1.0	∞	∞	17.424	4.558	3.951	1.562	2.382	1.032

Table 2: The value of the event horizon that makes the Hawking temperature zero. The second column denotes the black hole mass value at that radius.

Next, we compute the entropy using the first law of black hole thermodynamics, $S = \int \frac{dM}{T}$. We find

$$S = \pi r_H^2 = \frac{A}{4}. \quad (14)$$

We note that the PFDM and the dark energy do not affect the entropy of the event horizon which is consistent with the existing findings in the literature [78].

Now, we move on to explore phase transitions and stability. To achieve our purpose, we examine the heat capacity function

$$C = \frac{dM}{dT}, \quad (15)$$

in the presence of PFDM and dark energy. Taking into account Eqs. (9) and (11), Eq. (15) gives the heat capacity function in the form of

$$C = -2\pi r_H^2 \frac{1 + \frac{\alpha}{r_H} + \frac{3\sigma\omega_q}{r_H^{1+3\omega_q}}}{1 + \frac{2\alpha}{r_H} + \frac{3\sigma\omega_q(3\omega_q+2)}{r_H^{1+3\omega_q}}}. \quad (16)$$

It is remarkable that for $\alpha = \sigma = 0$ the capacity function returns to its standard form.

In Fig. 5 we display the variation of the heat capacity versus the event horizon for the chosen parameters above.

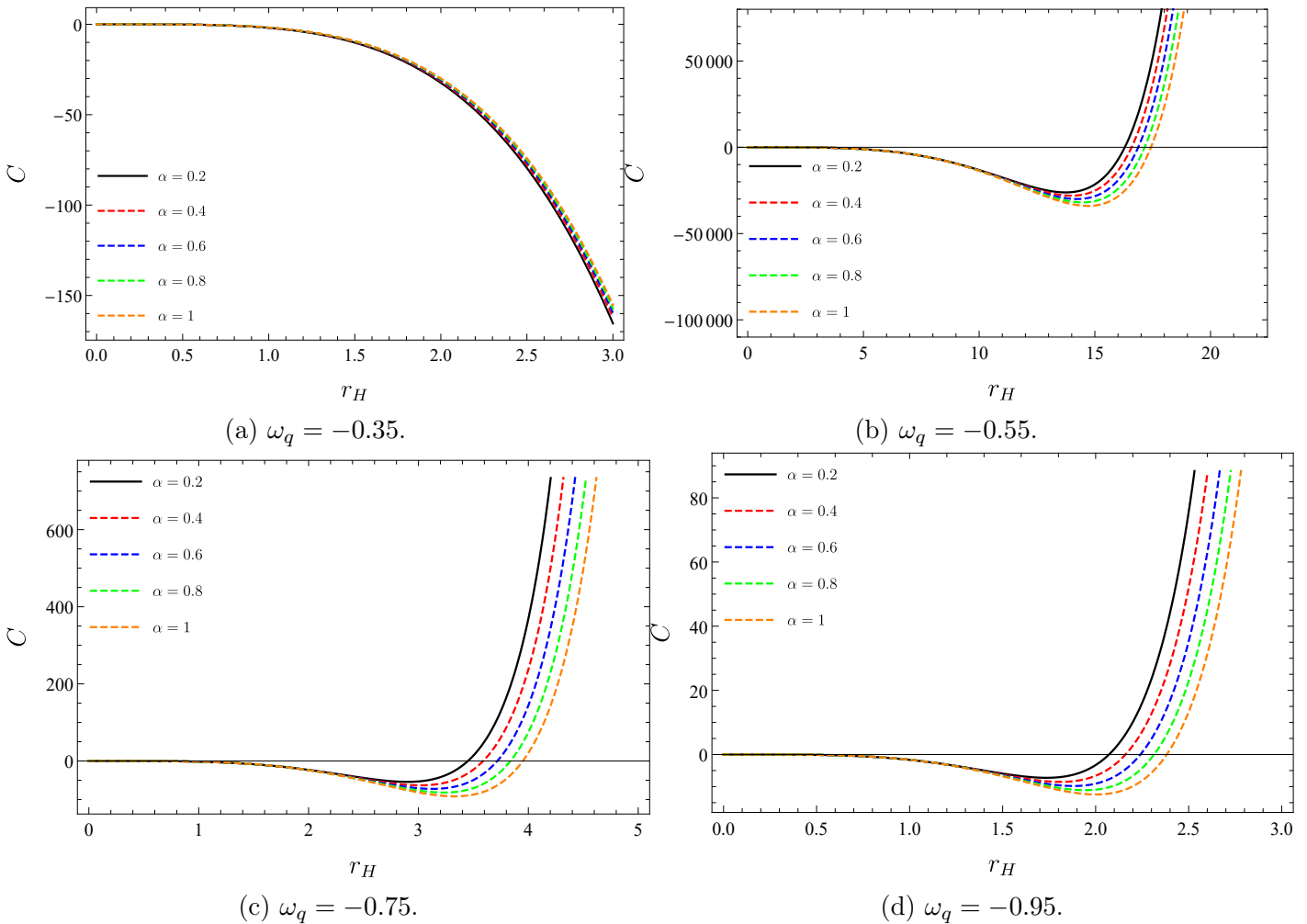


Figure 5: The impact of the dark matter and dark energy on the heat capacity function of Schwarzschild black hole for $\sigma = 0.1$.

As we emphasized before, we see that the $\omega_q = -0.35$ scenario differs from the other cases. Fig. 5a shows that the heat capacity function takes only negative values and the alteration of the dark matter parameters does not provide a significant modification. These findings mean that in this scenario the black hole is always thermally unstable [173]. In other cases, we observe that the heat capacity is first negative and then positive. This indicates a first-order phase transition at the horizon where specific heat equals zero. In other words, the vanishing value of the specific heat states that the black hole ceases to exchange radiation with its surroundings. Therefore, at that horizon black hole becomes stable and a remnant mass occurs. To clarify these discussions, we calculate the event horizon radii where specific heat disappears and present their values in Table 3.

α	$\omega_q = -0.35$	$\omega_q = -0.55$	$\omega_q = -0.75$	$\omega_q = -0.95$
	r_H	r_H	r_H	r_H
0.2	0	16.294	3.450	2.072
0.4	0	16.578	3.589	2.160
0.6	0	16.874	3.717	2.240
0.8	0	17.152	3.838	2.314
1.0	0	17.424	3.951	2.382

Table 3: Event horizon values where the heat capacity function equals zero.

We obtain two important results here. The first of these is that as the dark matter parameter increases, the event horizon radii also increase. Secondly, and more importantly, we see that the horizon values exactly coincide with those given in Table 2. This means that the mass values in Table 2 are the remnant masses.

Next, we examine the equation of state. To this end, we employ the relation between pressure and σ parameter

$$P = -\frac{\sigma}{8\pi}, \quad (17)$$

and rewrite the Hawking temperature in terms of pressure

$$P = -\frac{r_H^{1+3\omega_q}}{24\pi\omega_q} \left(1 + \frac{\alpha}{r_H} - 4\pi r_H T_H \right). \quad (18)$$

In Fig. 6, we display the pressure isotherms in terms of the horizon.

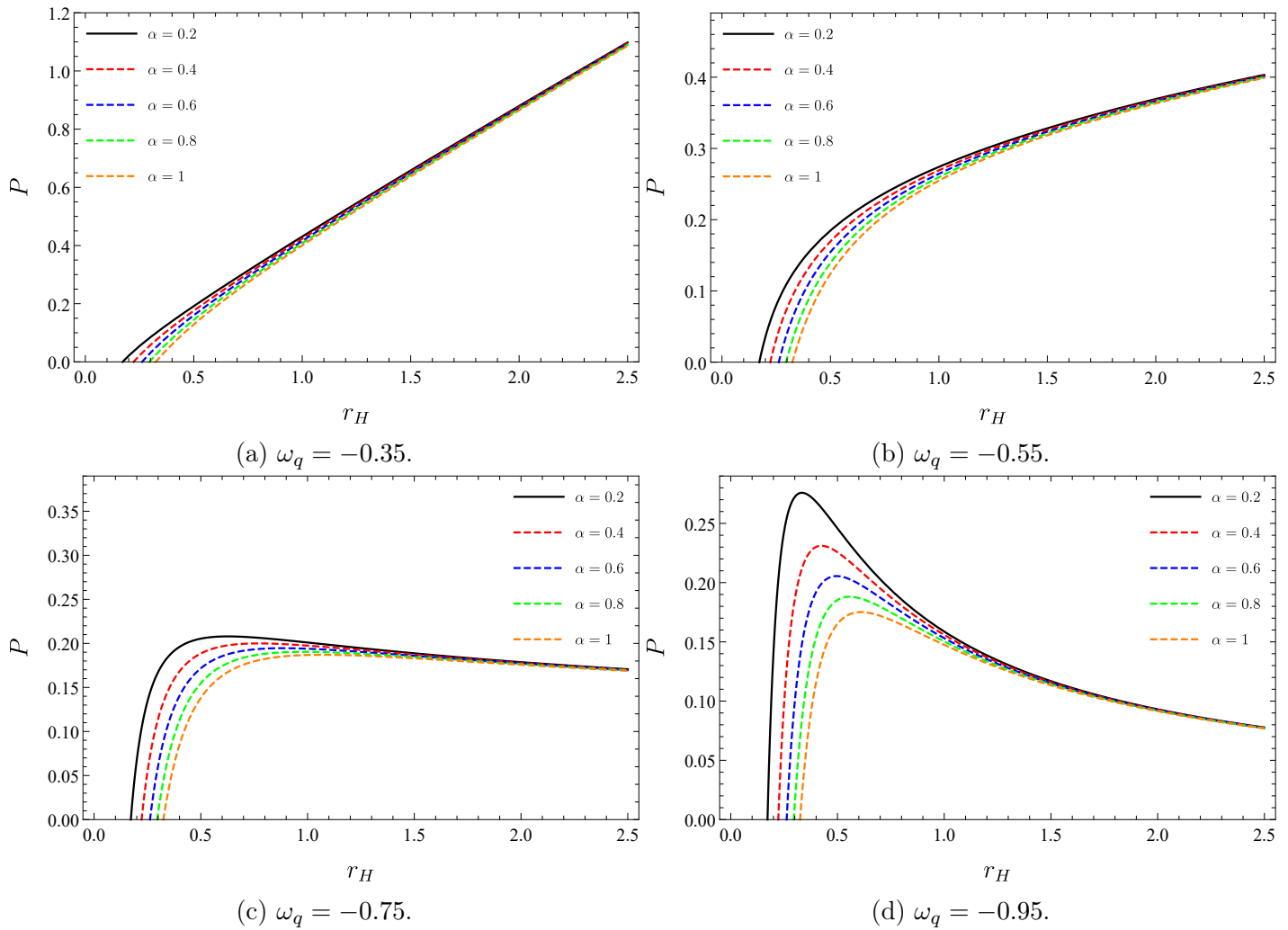


Figure 6: The impact of the dark matter on the pressure isotherms of $T = 1$.

We observe that dark matter alters the equation of state at relatively smaller horizons. This effect becomes significant for smaller quintessence state parameters. For example, in the case $\omega_q = -0.95$, the peak of the equation of state nearly disappears for greater dark matter parameters.

4 Black Hole's Shadow

In this section, we calculate the shape of the shadow cast of the black hole we are considering and investigate the effect of dark matter and quintessence field on these forms. To achieve our goal, we will derive the equation of motion using the Lagrangian formulation. Then, we will employ the Hamilton-Jacobi equation to study the geodesic equation near the black hole. We start with the Lagrangian,

$$\mathcal{L} = \frac{1}{2}g_{\mu\nu}\dot{x}^\mu\dot{x}^\nu, \quad (19)$$

where we use the dot notation over the variable to indicate differentiation with respect to the proper time. Here, for the static spacetime metric with spherical symmetry, we consider the Lagrangian of the form

$$\mathcal{L} = \frac{1}{2} \left[-f(r) \dot{t}^2 + \frac{1}{f(r)} \dot{r}^2 + r^2 \dot{\theta}^2 + r^2 \sin^2 \theta \dot{\phi}^2 \right], \quad (20)$$

Using the Euler-Lagrange equation

$$\frac{\partial \mathcal{L}}{\partial x^\mu} - \frac{d}{d\tau} \frac{\partial \mathcal{L}}{\partial \dot{x}^\mu} = 0, \quad (21)$$

we get two conserved quantities

$$\left(1 - \frac{2M}{r} - \frac{\sigma}{r^{3\omega_q+1}} + \frac{\alpha}{r} \ln \frac{r}{|\alpha|}\right) \dot{t} = E, \quad (22)$$

$$r^2 \sin^2 \theta \dot{\varphi} = L, \quad (23)$$

where E is the energy of the test particle and L is the angular momentum. Then, we analyze the orbits of photons around the black hole with the help of the Hamilton-Jacobi equation

$$\frac{\partial}{\partial \tau} \mathcal{S} = -\frac{1}{2} g_{\mu\nu} \frac{\partial \mathcal{S}}{\partial x^\mu} \frac{\partial \mathcal{S}}{\partial x^\nu}, \quad (24)$$

where the Jacobi action is denoted with \mathcal{S} . We then form the geodesic equations via Carter's approach [180]

$$\mathcal{S} = \frac{1}{2} m^2 \tau - Et + \mathcal{S}_r(r) + \mathcal{S}_\theta(\theta) + L\varphi, \quad (25)$$

Using this separation of variables we acquire the equation of motion of photons

$$-\frac{E^2}{f(r)} + f(r) \left(\frac{\partial \mathcal{S}_r}{\partial r}\right)^2 + \frac{1}{r^2} \left(\frac{\partial \mathcal{S}_\theta}{\partial \theta}\right)^2 + \frac{L^2}{r^2 \sin^2 \theta} = 0. \quad (26)$$

Now, we employ the relationships $P_\theta = \frac{\partial \mathcal{L}}{\partial \dot{\theta}} = \frac{\partial}{\partial \theta} \mathcal{S}_\theta$ and $P_r = \frac{\partial \mathcal{L}}{\partial \dot{r}} = \frac{\partial}{\partial r} \mathcal{S}_r$, and we obtain

$$\frac{\partial}{\partial \theta} \mathcal{S}_\theta = r^2 \dot{\theta}, \quad (27)$$

$$\frac{\partial}{\partial r} \mathcal{S}_r = \frac{1}{f(r)} \dot{r}. \quad (28)$$

Substituting Eqs. (27) and (28) in Eq. (26), we find two separated equations with the following form

$$r^4 \dot{r}^2 = r^4 E^2 - r^2 \left(1 - \frac{2M}{r} - \frac{\sigma}{r^{3\omega_q+1}} + \frac{\alpha}{r} \ln \frac{r}{|\alpha|}\right) (\mathcal{K} + L^2), \quad (29)$$

$$r^4 \dot{\theta}^2 = \mathcal{K} - L^2 \cot^2 \theta. \quad (30)$$

Here, \mathcal{K} is Carter's the separation constant. We then express the complete null geodesic equation

$$\dot{t} = \frac{E}{f(r)}, \quad (31)$$

$$\dot{\varphi} = \frac{L}{r^2 \sin^2 \theta}, \quad (32)$$

$$r^2 \dot{r} = \pm \sqrt{\mathcal{R}}, \quad (33)$$

$$r^2 \dot{\theta} = \pm \sqrt{\Theta}, \quad (34)$$

where

$$\mathcal{R} = r^4 E^2 - r^2 (\mathcal{K} + L^2) \left(1 - \frac{2M}{r} - \frac{\sigma}{r^{3\omega_q+1}} + \frac{\alpha}{r} \ln \frac{r}{|\alpha|}\right), \quad (35)$$

$$\Theta = \mathcal{K} - L^2 \cot^2 \theta. \quad (36)$$

We observe that two impact parameters characterize photon motion in the vicinity of the black hole

$$\eta = \frac{L}{E}, \quad (37)$$

$$\zeta^2 = \frac{\mathcal{K}}{E^2}, \quad (38)$$

which depends on the constants of motion and Carter's separation constant. These impact parameters govern key properties of the photon's trajectory influenced by the gravitational field of the black hole.

We now focus on the unstable circular orbits of photons that encode the boundaries of shadow casts. To find these boundaries, we revisit the equation that describes the radial motion of photons

$$\dot{r}^2 + V_{eff}(r) = 0, \quad (39)$$

with the effective potential of the radial motion

$$V_{eff}(r) = \left(\frac{\mathcal{K} + L^2}{r^2} \right) \left(1 - \frac{2M}{r} - \frac{\sigma}{r^{3\omega_q+1}} + \frac{\alpha}{r} \ln \frac{r}{|\alpha|} \right) - E^2. \quad (40)$$

Due to three possible trajectories of photons approaching the black hole, namely falling into it, scattering away, or forming a circular orbit near the black hole, the shape of the shadow is influenced primarily by the unstable circular orbits. We can identify these orbits by imposing the following conditions

$$V_{eff}(r)|_{r=r_{ph}} = 0, \quad (41)$$

and

$$\left. \frac{d}{dr} V_{eff}(r) \right|_{r=r_{ph}} = 0, \quad (42)$$

with

$$\left. \frac{d^2}{dr^2} V_{eff}(r) \right|_{r=r_p} < 0, \quad (43)$$

which indicates a maxima for the effective potential at $r = r_{ph}$. At first, we use Eq. (41) and find

$$\eta + \zeta^2 = \frac{r_{ph}^2}{1 - \frac{2M}{r_{ph}} - \frac{\sigma}{r_{ph}^{3\omega_q+1}} + \frac{\alpha}{r_{ph}} \ln \frac{r_{ph}}{|\alpha|}}. \quad (44)$$

Then, we utilize Eq. (42), and obtain a relationship

$$r_{ph} f'(r_{ph}) - 2f(r_{ph}) = 0, \quad (45)$$

in terms of r_{ph} . After we substitute the lapse function, Eq. (7), we arrive at a subsequent equation

$$2 - \frac{6M}{r_{ph}} - \frac{\sigma(3\omega_q + 3)}{r_{ph}^{3\omega_q+1}} + \frac{3\alpha}{r_{ph}} \ln \frac{r_{ph}}{|\alpha|} - \frac{\alpha}{r_{ph}} = 0. \quad (46)$$

This equation describing the photon sphere has no analytical solution, so we have to resort to numerical methods to reach the solution. We tabulate the calculated photon sphere radii and the impact parameter of the photon sphere, $\eta + \zeta^2$, for different values of dark matter and quintessence field state parameters in Table 4.

α	$\omega_q = -0.35$		$\omega_q = -0.55$		$\omega_q = -0.75$		$\omega_q = -0.95$	
	r_p	$\eta + \zeta^2$						
0.2	2.59645	20.9170	2.66310	20.9574	2.66306	20.9573	2.44482	21.1831
0.4	2.37328	15.9573	2.41058	15.9696	2.39378	15.9611	2.24088	16.1484
0.6	2.31904	14.0390	2.34807	14.0461	2.33044	14.0401	2.20121	14.1805
0.8	2.34719	13.4236	2.37539	13.4300	2.36056	13.4251	2.23941	13.5350

Table 4: The values of the photon radius, r_p , and $\eta + \zeta^2$ for different values of α and ω_q with $\sigma = 0.1$ and $M = 1$.

We now introduce Celestial coordinates, X and Y , to describe the actual shadow of the black hole seen in an observer's frame [172]

$$X = \lim_{r_o \rightarrow \infty} \left(-r_o^2 \sin \theta_o \frac{d\varphi}{dr} \right), \quad (47)$$

$$Y = \lim_{r_o \rightarrow \infty} \left(r_o^2 \frac{d\theta}{dr} \right). \quad (48)$$

Here, r_o is the location of the observer, and θ_o is the angle of inclination. Using the geodesics equations, we simplify Eqs. (47) and (48) to a simpler form

$$X = -\frac{\zeta}{\sin \theta_0}, \quad (49)$$

$$Y = \sqrt{\eta - \zeta^2 \cot^2 \theta_0}. \quad (50)$$

The preceding two equations establish a connection between the celestial coordinates and the constants of motion. We then consider the equatorial plane with $\theta_0 = \pi/2$, so the celestial coordinates simplify to

$$X^2 + Y^2 = \eta + \zeta^2 = R_S^2. \quad (51)$$

Here, R_S is the radius of the shadow.

Now, we display the effect of the PFDM and quintessence matter field on the black hole shadows. First, in Fig. 7 we present the impact of dark matter with four distinguished dark energy scenarios. We observe that for smaller dark matter parameters the shadows have greater radii.

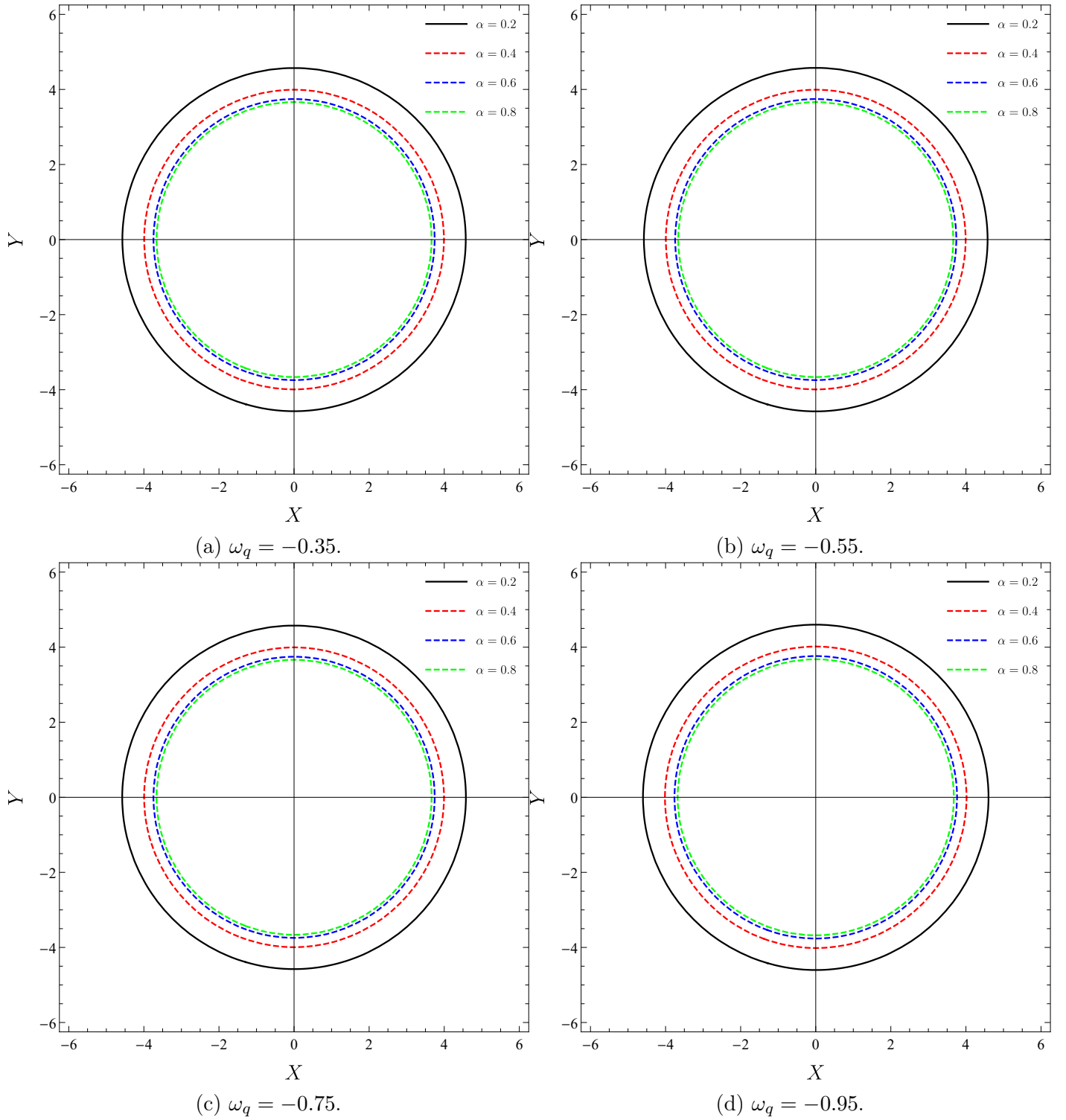


Figure 7: The impact of the dark matter on the shadows of the Schwarzschild black with $M = 1$ and $\sigma=0.1$.

However, in these graphs, we cannot clarify the effect of the quintessence matter field in a fixed dark matter scenario. To explain this, we plot Fig. 8.

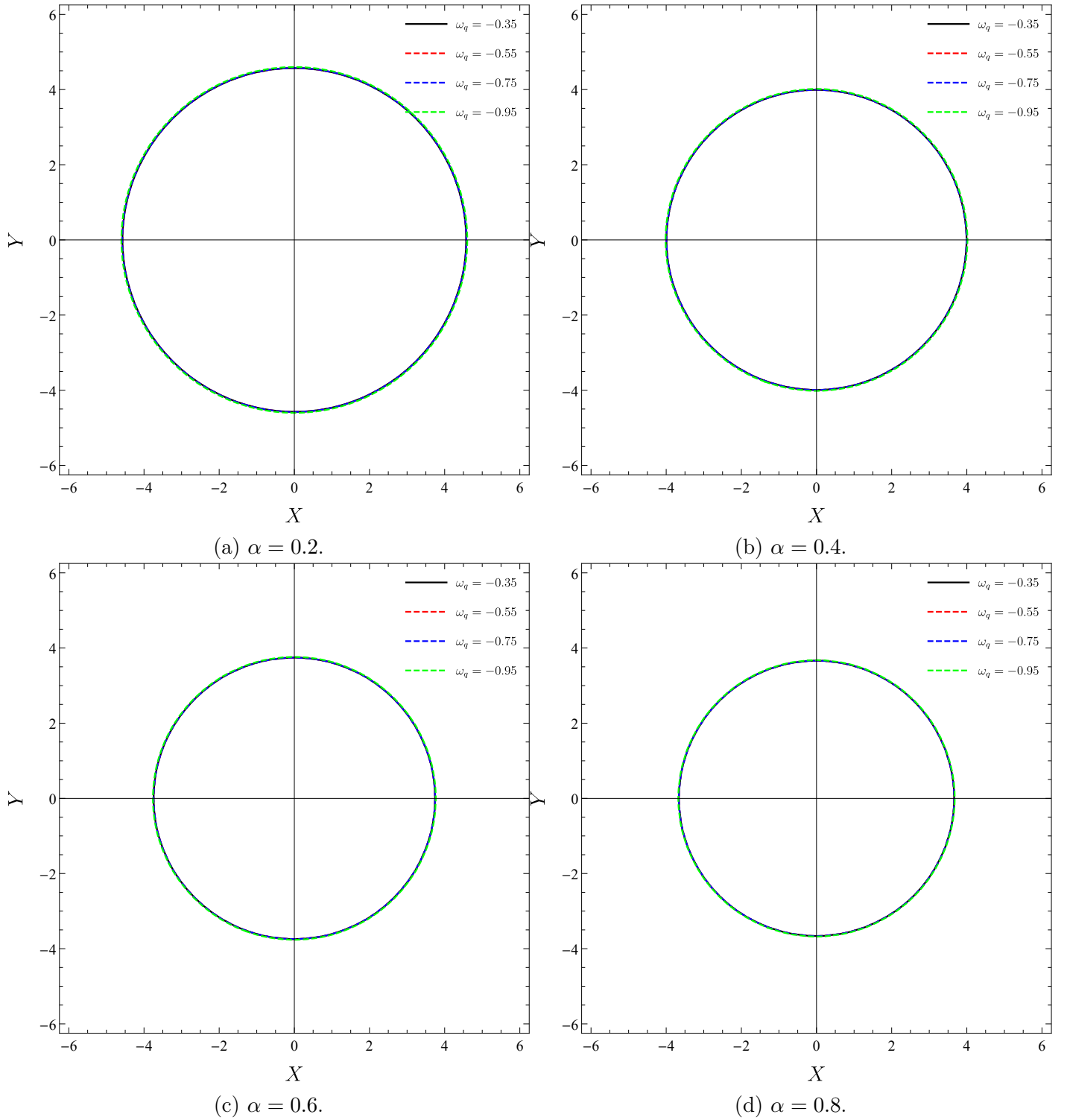


Figure 8: The impact of the dark energy on the shadows of the Schwarzschild black with $M = 1$ and $\sigma=0.1$.

We observe that the influence of the quintessence matter field on the shadow radius is limited. We revisit these effects in Fig. 9.

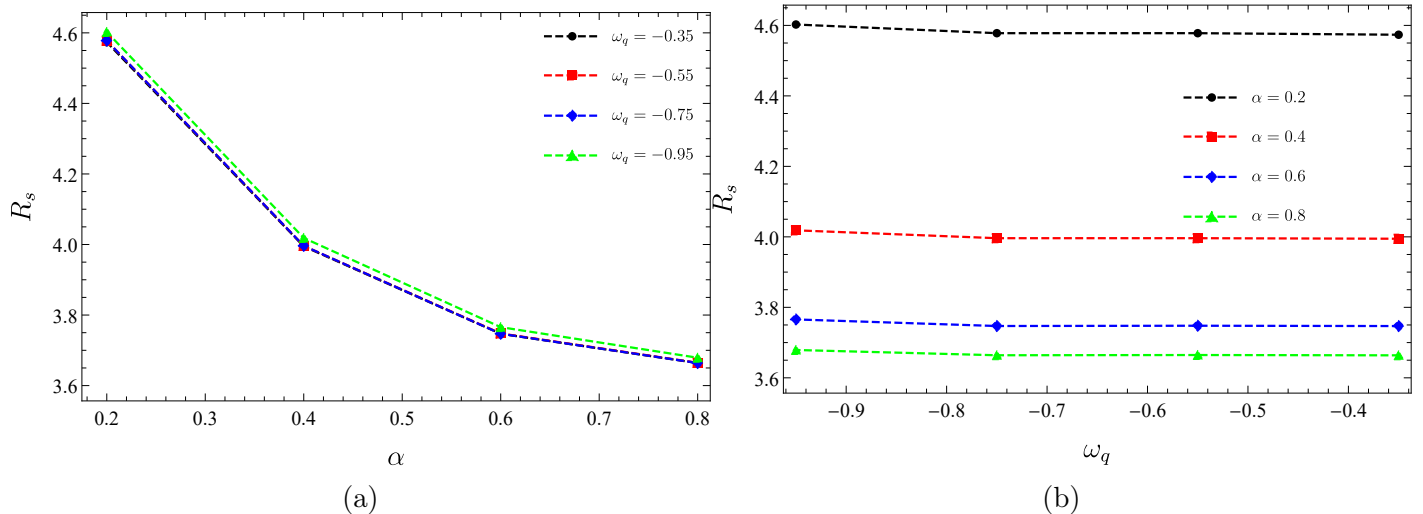


Figure 9: The variation of the radius of the black hole shadow for fixed M and σ values.

Fig. 9a displays that an increase in the dark matter parameter leads to a decrease in the shadow radius. We observe that this impact is the same for all quintessence matter cases. Fig. 9b shows that the shadow radius slightly decreases as the quintessence matter increases for a fixed dark matter parameter.

5 Black Hole's Quasinormal Modes

After a significant event such as the merger of black holes, the ringdown phase exhibits an intriguing behavior called quasinormal modes. These modes display distinct oscillation patterns not influenced by the initial disturbances that caused them. In other words, the quasinormal modes arise from the intrinsic properties of the system itself, representing the natural vibrations of spacetime, irrespective of the precise initial conditions that triggered them. They gradually emit energy through gravitational waves and they are associated with open systems, as opposed to normal modes, which are linked to closed systems.

In the literature, we observe distinct methodologies for the calculation of their frequencies [174–179]. One of the most preferred ones requires these modes by solving the wave equation within the context of a system defined by a background metric. However, deriving analytical solutions for these modes is often an extremely challenging endeavor, and various approaches are used to obtain them. Among these, the Wentzel-Kramers-Brillouin (WKB) approach stands out with its widespread use.

5.1 WKB approach

The WKB was initially proposed in [181, 182] at the first order, and subsequently extended to higher orders by Iyer, Opala, and Konoplya [183–185]. The WKB approach gained popularity in recent decades because, unlike more advanced numerical methods, it automatically applies to diverse effective potentials with sufficient accuracy.

Our purpose here is to consider the massless scalar quasinormal mode in the Schwarzschild spacetime surrounded by quintessence in the background of PFDM. We start with the Klein-Gordon differential equation of the curved spacetime

$$\frac{1}{\sqrt{-g}}\partial_\mu(\sqrt{-g}g^{\mu\nu}\partial_\nu\psi) = 0, \quad (52)$$

to describe the propagation of the massless scalar field, ψ . By taking the spherical symmetry into

account, we decompose the scalar field in a specific manner

$$\psi(t, r, \theta, \varphi) = e^{-i\omega t} \frac{\Psi_{\omega, L}(r)}{r} Y_{L, \mu}(\theta, \varphi), \quad (53)$$

where ω and $Y_{L, \mu}(\theta, \varphi)$ denote the frequency and the spherical harmonics, respectively. Then, we substitute this decomposition in Eq. (52), and get a Schrodinger-like equation that exhibits wave-like properties,

$$\frac{d^2}{dr^{*2}} \Psi(r^*) - (\omega^2 - V(r^*)) \Psi(r^*) = 0. \quad (54)$$

Here, we use the tortoise variable

$$dr^* = \frac{dr}{f(r)}, \quad (55)$$

with the Regge-Wheeler potential

$$V(r) = \frac{f(r)}{r} \frac{df(r)}{dr} + \frac{f(r)}{r} \frac{L(L+1)}{r}. \quad (56)$$

Now, we utilize Eq. 7 and depict the Regge-Wheeler potential with different dark matter and quintessence state parameter values in Fig. 10.

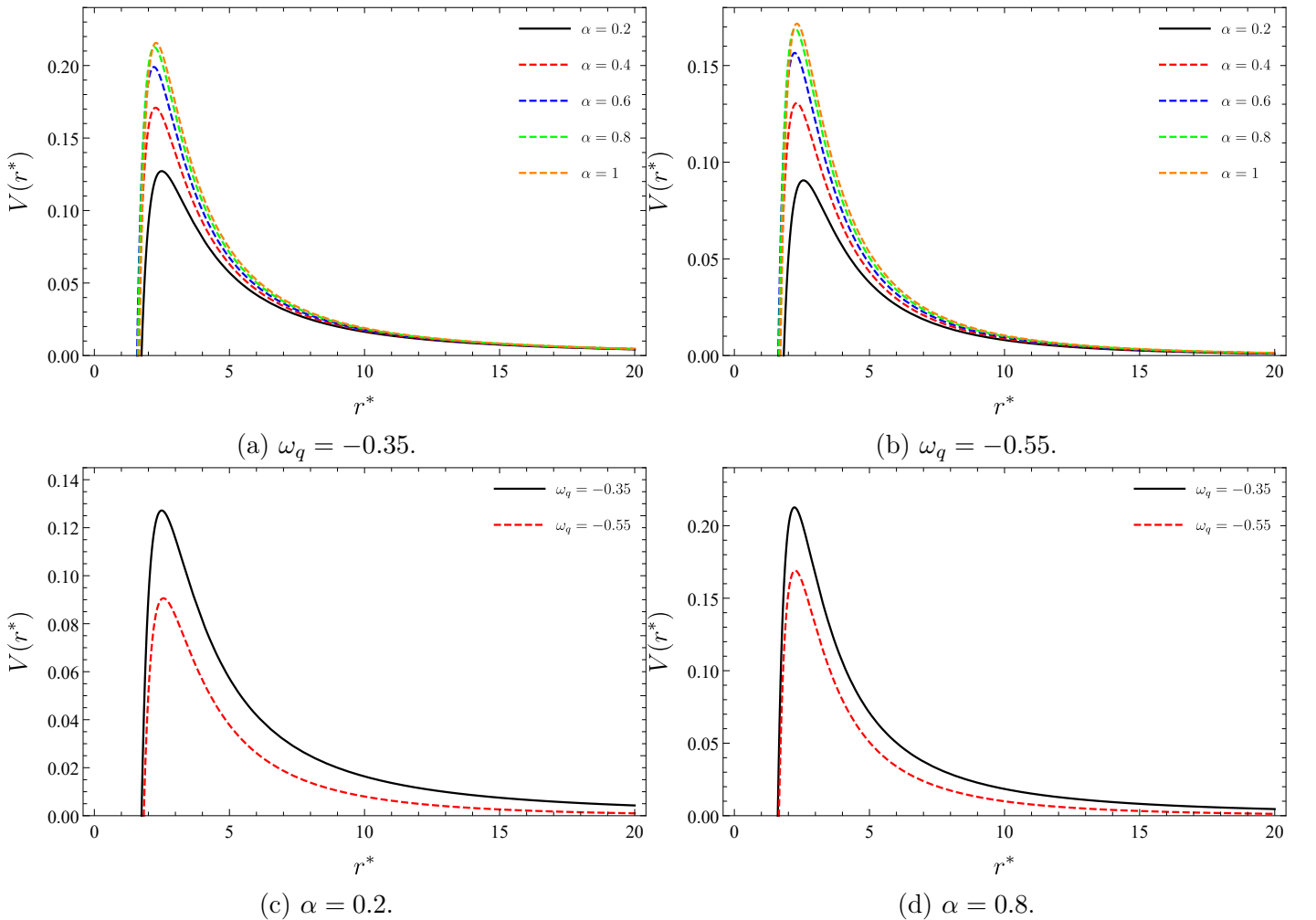


Figure 10: Regge-Wheeler potential in terms of r^* for different values of α and ω_q with $M = 1$ and $\sigma = 0.1$.

Figs. 10a and 10b show that the peak of the potential becomes significant as the dark matter parameter increases. However, this behavior does not notably alter in the distinct scenarios of quintessence matter fields as indicated in Figs. 10c and 10d.

Now, we solve Eq. (54) under the specified boundary condition

$$\Psi \simeq e^{\pm i\omega r^*}, \quad r^* \rightarrow \pm\infty, \quad (57)$$

for determining the quasinormal modes. Here, we have to emphasize that the WKB approach can be valid if and only if the potential has a barrier-like shape and tends to constant values as $r^* \rightarrow \pm\infty$. After fitting the power series solution near the potential's turning points, we get the quasinormal modes generator in the form of [185]

$$i \frac{(\omega_n - V_0)}{\sqrt{-2V_0''}} - \sum_{i=2}^N \Lambda_i = n + \frac{1}{2}. \quad (58)$$

Here, n is the overtone numbers that take only integer values. V_0 is the effective potential height and V_0'' is the second derivative to the tortoise coordinate of the potential at its maximum r_0^* . Λ_i is a constant coefficient resulting from higher-order WKB corrections and its explicit expressions were given in [184, 185] for the higher orders. Then, with the sixth-order WKB method we calculate the quasinormal frequencies and present them in Table 5.

$\alpha = 0.2$					
L	n	$\omega_q = -0.35$	$\omega_q = -0.55$	$\omega_q = -0.75$	$\omega_q = -0.95$
1	0	0.286697-0.130367 i	0.243049-0.102204 i	0.167207-0.062235 i	0.088169-0.217382 i
2	0	0.522059-0.116583 i	0.452545-0.094832 i	0.291393-0.058030 i	0.082422-0.367061 i
	1	0.472045-0.383570 i	0.419863-0.313977 i	0.301527-0.178605 i	0.242275-0.408652 i
3	0	0.748478-0.113292 i	0.648638-0.092489 i	0.414522-0.056541 i	0.079722-0.519477 i
	1	0.740130-0.369166 i	0.642165-0.300088 i	0.417317-0.174583 i	0.241083-0.543687 i
	2	0.617352-0.665079 i	0.562526-0.546217 i	0.434059-0.296269 i	0.397733-0.598888 i
4	0	0.971106-0.111910 i	0.841437-0.091495 i	0.536739-0.055883 i	0.078399-0.671671 i
	1	0.963634-0.356097 i	0.832598-0.292034 i	0.536914-0.171503 i	0.238350-0.687398 i
	2	0.933763-0.644846 i	0.815571-0.521053 i	0.545181-0.292983 i	0.399276-0.726612 i
	3	0.734400-0.931059 i	0.683972-0.773060 i	0.566755-0.414447 i	0.553285-0.789731 i
$\alpha = 0.5$					
1	0	0.310951-0.146376 i	0.282983-0.124096 i	0.251959-0.114566 i	0.013906-0.0315182 i
2	0	0.612428-0.150235 i	0.552881-0.129377 i	0.442171-0.102615 i	0.013290-0.0535657 i
	1	0.511360-0.479501 i	0.474381-0.420532 i	0.416412-0.448855 i	0.038497-0.0587866 i
3	0	0.886533-0.147911 i	0.799762-0.127860 i	0.630862-0.099104 i	0.012929-0.0759021 i
	1	0.863738-0.488408 i	0.782596-0.421004 i	0.629265-0.336559 i	0.038831-0.0789541 i
	2	0.641399-0.799494 i	0.605289-0.708823 i	0.492779-0.596203 i	0.063048-0.0857387 i
4	0	1.153270-0.146388 i	1.040150-0.126681 i	0.817836-0.097655 i	0.0127326-0.098205 i
	1	1.141960-0.471496 i	1.030190-0.406636 i	0.813113-0.311049 i	0.0386125-0.100088 i
	2	1.058440-0.854819 i	0.969550-0.735938 i	0.794382-0.576247 i	0.0640501-0.105080 i
	3	0.752816-1.083220 i	0.715545-0.969873 i	0.576455-0.836921 i	0.0874828-0.112720 i

Table 5: The quasinormal modes for the massless scalar perturbation with $M = 1$, and $\sigma = 0.1$ via the Pade averaged 6th order WKB approximation method.

In Fig. 11 and Fig. 12 we compare the real and imaginary parts of the quasinormal modes.

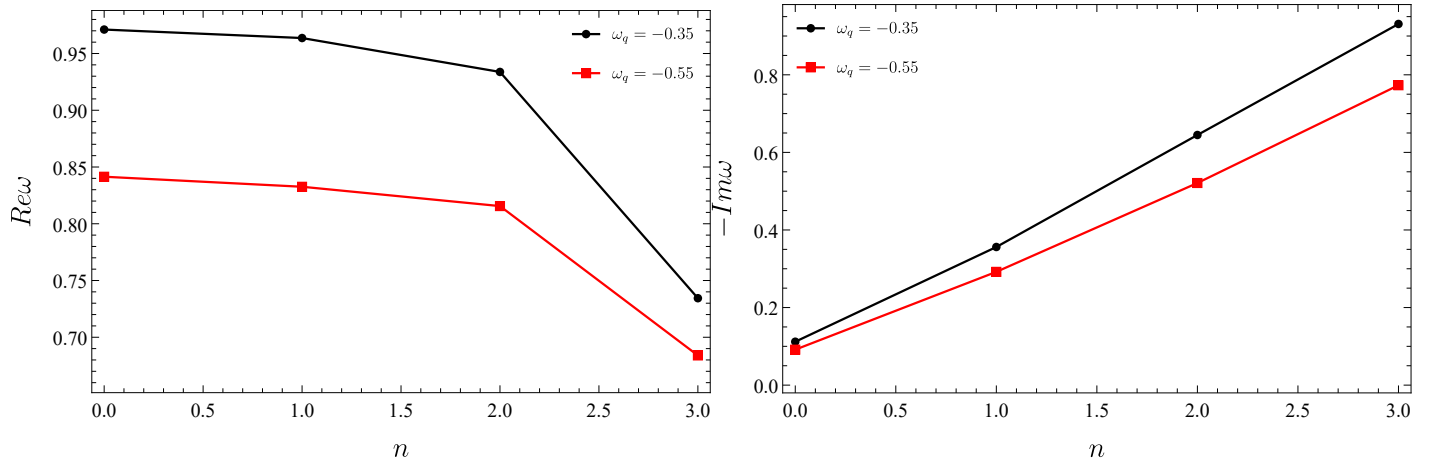


Figure 11: The variation of the $Re\omega$ and $Im\omega$ versus overtone numbers for two values of $\omega_q = -0.35$, $\omega_q = -0.55$, with $M = 1$, $\alpha = 0.2$, $L = 4$.

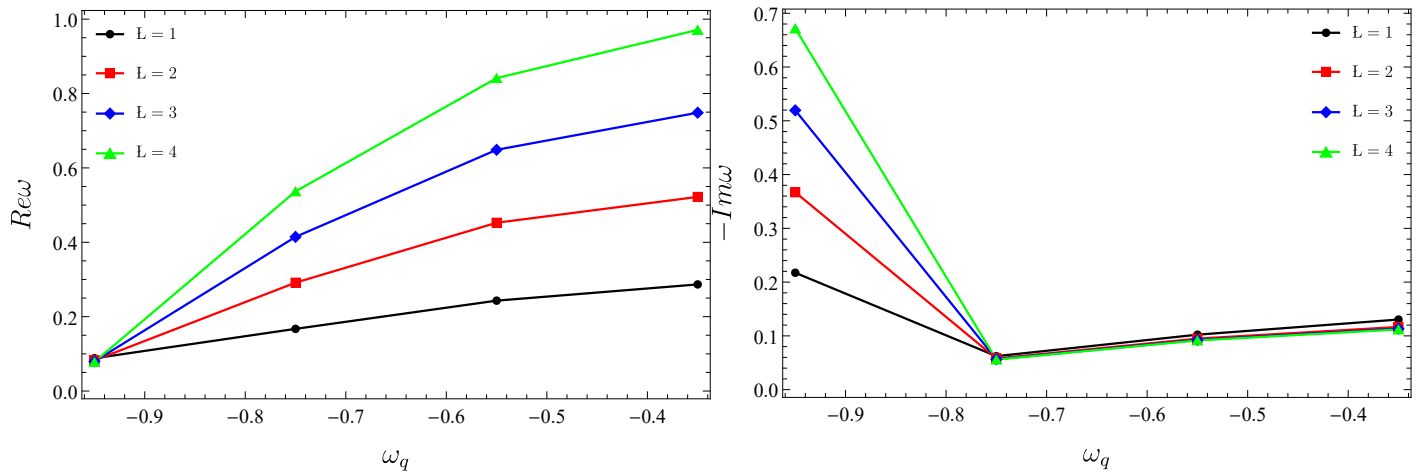


Figure 12: The variation of the $Re\omega$ and $Im\omega$ vs. ω_q for $n = 0$, $\alpha = 0.2$, $\sigma = 0.1$ and $M = 1$.

We note that the real section of frequencies decreases for greater n , while the imaginary section increases. We observe that the real section of quasinormal modes increases at greater values of the quintessence state parameter. Moreover, for greater L this enlargement expands. However, in the imaginary sector, we observe a decrease at first, and then the quasinormal modes increase for greater values of the quintessence state parameter.

The importance of the WKB order becomes evident in determining accurate values of QNM frequencies. The quantity for ω_k , derived through the WKB formula of order " k " for each overtone n , is defined as

$$\Delta = \frac{|\omega_{k-1} - \omega_{k+1}|}{2}. \quad (59)$$

We compute the quasinormal frequencies and the estimated errors for $L = 1$ and $n = 0$. We present the results in Table 6.

k	$\alpha = 0.2$		$\alpha = 0.4$	
	ω_k	Δ_k	ω_k	Δ_k
3	0.115987-0.0457716 i	0.00179603	0.202929-0.0897261 i	0.00269626
4	0.11512-0.04104750 i	0.00256651	0.207087-0.0829896 i	0.00494956
5	0.114298-0.0423931 i	0.00121871	0.198699-0.0839376 i	0.00418022
6	0.116721-0.0426669 i	0.00079614	0.205075-0.0852250 i	0.00164852
7	0.115464-0.0423223 i	0.00059041	0.204147-0.0838090 i	0.00165888
8	0.115525-0.0428855 i	0.00100064	0.203483-0.0855179 i	0.00139755
9	0.116151-0.0422390 i	0.00047425	0.204282-0.0841058 i	0.00115333
10	0.115810-0.0426108 i	0.00030129	0.203774-0.0838807 i	0.00084838
11	0.115923-0.0427487 i	0.00078338	0.203652-0.0841582 i	0.00033406
12	0.115919-0.0425271 i	0.00015844	0.203824-0.0838608 i	0.00079516
13	0.115959-0.0426456 i	0.00034563	0.203382-0.0838610 i	0.00081246

Table 6: Quasinormal modes and error estimations for $M = 1$, $\sigma = 0.1$, $\omega_q = -0.80$, $L = 1$, and $n = 0$ through different orders of the WKB approach.

5.2 Mashhoon approximation

In [186], Mashhoon proposed to use Pösch-Teller (PT) potential for calculating the quasinormal modes

$$\mathcal{V}(r^*) \sim V_{PT}(r^*) = \frac{V_0}{\cosh^2 \beta (r^* - r_0^*)}, \quad (60)$$

where

$$\beta = \sqrt{-\frac{1}{2V_0} \frac{d^2 \mathcal{V}(r^*)}{dr^{*2}} \Big|_{r^*=r_0^*}}. \quad (61)$$

Here, r_0^* is the position of the maximum of $\mathcal{V}(r^*)$ where $\mathcal{V}(r_0^*) = V_0$. The quasinormal modes of the Pösch-Teller (PT) potential can be computed analytically

$$\omega_n = \pm \beta \sqrt{\frac{V_0}{\beta^2} - \frac{1}{4}} - i\beta \left(n + \frac{1}{2} \right). \quad (62)$$

We apply this solution to calculate the quasinormal modes with different dark matter parameter values. We tabulate the results for the scalar field in Table 7. Moreover, we compare them with the frequencies obtained through the 3rd-order WKB method.

α	$\omega_q = -0.40$		$\omega_q = -0.60$	
	WKB method	Mashhoon approximation	WKB method	Mashhoon approximation
0.3	0.329678-0.117361 i	0.356702-0.125127 i	0.284959-0.095995 i	0.297511-0.103264 i
0.4	0.348387-0.128153 i	0.378995-0.137513 i	0.306336-0.107298 i	0.322028-0.116113 i
0.5	0.361048-0.137034 i	0.395447-0.148050 i	0.320987-0.116472 i	0.339968-0.126847 i
0.6	0.368699-0.144095 i	0.406926-0.156764 i	0.330112-0.123658 i	0.352384-0.135553 i
0.7	0.372336-0.149506 i	0.414282-0.163773 i	0.334837-0.129067 i	0.360273-0.142399 i
0.8	0.372844-0.153473 i	0.418299-0.169246 i	0.336148-0.132941 i	0.364530-0.147595 i

Table 7: The comparison of the quasinormal modes estimated with the Mashhoon approximation and 3rd order WKB method, for specific parameters: $M = 1$, $L = 1$, $n = 0$, $\sigma = 0.1$, and varying values of the parameter α .

Finally, we present a graphical comparison in Fig. 13.

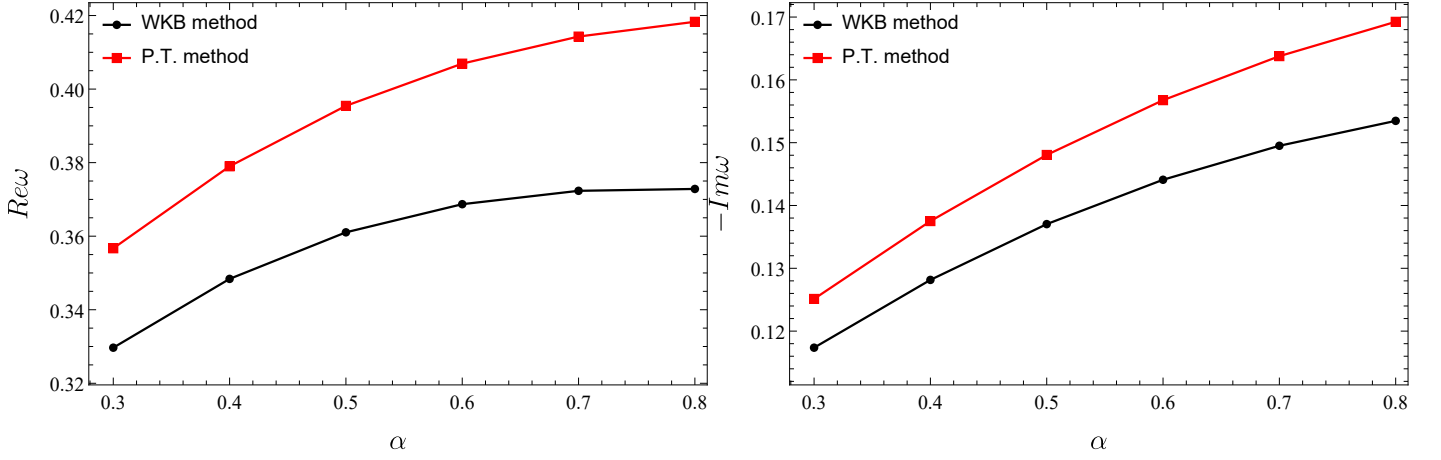


Figure 13: Qualitative comparison of the Mashhoon and WKB approximations with $M = 1$, $\sigma = 0.1$, $L = 1$, $n = 0$, $\omega_q = -0.4$ and varying values of α parameter.

6 Conclusions

In this paper, we handled the Schwarzschild black hole surrounded by PFDM in the presence of the quintessence matter field, and we explored its thermodynamics, shadows, and quasinormal modes. To this end, we initially derived the lapse function of the black hole and discussed the lapse function's characteristics in four different quintessence field scenarios. We found that the quintessence matter field significantly alters the behavior of the lapse function unless the quintessence state parameter is large enough. Then, we examined the mass function. We observed that dark matter sets a lower limit on the event horizon, but also expands its upper bound value. We noted that achieves a maximum mass value at a larger event horizon with a greater dark matter parameter. Next, we examined the black hole's thermodynamics. At first, We derived the modified Hawking temperature. We found that it tends to zero unless the quintessence state parameter is not large enough. We showed the event horizon entropy is not affected by dark matter and quintessence matter field. Then. we investigated the heat capacity function. We showed that except very large quintessence state parameter case, the black hole has a first-order phase transition. In these cases, the black hole stops exchanging radiation with its surroundings and becomes stable with a remnant mass. Then, we derived the equation of state function and discussed the pressure isotherms. Next, we investigated the shadow casts through Carter's approach, We obtained the null geodesic equations to describe the photon motion. Then, we found the effective potential and showed the impacts of dark matter and quintessence matter fields on it. We demonstrated the shadows in celestial coordinates. We found that dark matter significantly lessens the shadow radius, while quintessence matter does not. Finally, we studied the quasinormal modes with the WKB and Mashhoon approximations. We tabulated quasinormal frequencies and showed the impact of dark matter and quintessence matter fields.

Acknowledgments

B. C. L. is grateful to Excellence Project PřF UHK 2211/2023-2024 for the financial support.

Data Availability Statements

The authors declare that the data supporting the findings of this study are available within the article.

References

- [1] G. Bertone, D. Hooper, *Rev. Mod. Phys.* **90**, 045002 (2018).
- [2] D. Huterer, D. L. Shafer, *Rep. Prog. Phys.* **81**, 016901 (2018).
- [3] F. Rahaman, K. K. Nandi, A. Bhadra, M. Kalam, K. Chakraborty, *Phys. Lett. B* **694**, 10 (2010).
- [4] A. A. Potapov, G. M. Garipova, K. K. Nandi, *Phys. Lett. B* **753**, 140 (2016).
- [5] V. C. Rubin, W. K. Ford, *Astrophys. J.* **159**, 379 (1970).
- [6] M. S. Roberts, A. H. Rots, *Astron. Astrophys.* **26**, 483 (1973).
- [7] V. C. Rubin, W. K. Ford Jr., N. Thonnard, *Astrophys. J.* **238**, 471 (1980).
- [8] J. P. Ostriker, P. J. E. Peebles, *Astrophys. J.* **186**, 467 (1973).
- [9] J. Einasto, A. Kaasik, F. Saar, *Nature* **250**, 309 (1974).
- [10] M. Davis, G. Efstathiou, C. S. Frenk, S. D. M. White, *Astrophys. J.* **292**, 371 (1985).
- [11] D. Clowe, M. Bradac, A. H. Gonzalez, M. Markevitch, S. W. Randall, C. Jones, D. Zaritsky, *Astrophys. J.* **648**, L109 (2006).
- [12] R. Mandelbaum et al., *Mon. Not. R. Astron. Soc.* **432**, 1544 (2013).
- [13] G. Hinshaw et al., (WMAP Collaboration) *Astrophys. J. Suppl.* **208**, 19 (2013).
- [14] P. A. R. Ade et al., (Planck Collaboration), *Astron. Astrophys.* **571**, A16 (2014).
- [15] E. Komatsu et al., (WMAP Collaboration), *Astrophys. J. Suppl.* **192**, 18 (2011).
- [16] I. de Martino, S.S. Chakrabarty, V. Cesare, A. Gallo, L. Ostorero, A. Diaferio, *Universe* **6**, 107 (2020).
- [17] P. Salucci, N. Turini, C. di Paolo, *Universe* **6**, 118 (2020).
- [18] A. Filippi, M. de Napoli, *Rev. Phys.* **5**, 100042 (2020).
- [19] A. Arbey, F. Mahmoudi, *Progr. Particl. Nucl. Phys.* **119**, 103865 (2021),
- [20] E. Oks, *New Astron. Rev.* **93**, 101632 (2021).
- [21] E. Oks, *New Astron. Rev.* **96**, 101673 (2023).
- [22] J. F. Navarro, C. S. Frenk, S. D. M. White, *Astrophys. J.* **462**, 563 (1996).
- [23] C. Boehm, P. Fayet, *Nucl. Phys. B* **683**, 219 (2004).
- [24] G. Bertone, D. Hooper, J. Silk, *Phys. Rept.* **405**, 279 (2005).

- [25] J. L. Feng, M. Kaplinghat, H. Tu, H. -B. Yu, *JCAP* **2009**, 004 (2009).
- [26] P. W. Graham, I. G. Irastorza, S. K. Lamoreaux, A. Lindner, K. A. van Bibber, *Ann. Rev. Nucl. Part. Sci.* **65**, 485 (2015).
- [27] M. Schumann, *J. Phys. G: Nucl. Part. Phys.* **46**, 103003 (2019).
- [28] A. Boyarsky, M. Drewes, T. Lasserre, S. Mertens, O. Ruchayskiy, *Prog. Part. Nucl. Phys.* **104**, 1 (2019).
- [29] C. -K. Qiao, S. -T. Lin, H. -C. Chi, H. -T. Jia, *J. High Energ. Phys.* **2021**, 184 (2021).
- [30] A. Deur, *Eur. Phys. J. C* **79**, 883 (2019).
- [31] A. Yajalom, *Symmet.* **12**, 1693 (2020).
- [32] E. Oks, *Res. Astron. Astrophys.* **20**, 109 (2020).
- [33] E. Oks, *New Astron.* **107**, 102134 (2024).
- [34] V. V. Kiselev, arXiv: gr-qc / 0303031.
- [35] M. H. Li, K. C. Yang, *Phys. Rev. D* **86**, 123015 (2012).
- [36] Z. Xu, X. Hou, J. Wang, *Class. Quantum Grav.* **35**, 115003 (2018).
- [37] X. Hou. Z. Xu, J. Wang. *J. Cosmol. Astropart. Phys.* **12**, 040 (2018).
- [38] S. Haroon, M. Jamil, K. Jusufi, R. B. Mann, *Phys. Rev. D* **99**, 044015 (2019).
- [39] M. Rizwan, M. Jamil, K. Jusufi, *Phys. Rev. D* **99**, 024050 (2019).
- [40] S. H. Hendi, A. Nemati, K. Lin, M. Jamil, *Eur. Phys. J. C* **80**, 296 (2020).
- [41] F. Atamurotov, U. Papnoi, K. Jusufi, *Class. Quantum Grav.* **39**, 025014 (2022).
- [42] Z. Hu, X. Hou, J. Wang. Y. Liao, *Adv. High Energy Phys.* **2019**, 2434390 (2019).
- [43] F. Atamurotov, A. Abdujabbarov, W. -B. Han, *Phys. Rev. D* **104**, 084015 (2021).
- [44] J. Rajimbaev, S. Shaymatov, M. Jamil, *Eur. Phys. J. C* **81**, 699 (2021).
- [45] R. Ndongmo, S. Mahamat, C. B. Tabi, T. B. Bouetou, T. C. Kofane, *Phys. Dark Univ.* **42**, 101299 (2023).
- [46] G. Rakhimova, F. Atamurotov, F. Javed, A. Abdujabbarov, G. Mustafa, *Nucl. Phys. B* **996**, 116363 (2023).
- [47] C. -K. Qiao, M. Zhou, *J. Cosmol. Astropart. Phys.* **12**, 005 (2023).
- [48] A. Das, A. R. Chowdhury, S. Gangopadhyay, *Class. Quantum Grav.* **41**, 015018 (2024).
- [49] A. G. Riess et al., *Astronom. J.* **116**, 1008 (1998).
- [50] A. G. Riess et al., *Astronom. J.* **117**, 707 (1999).
- [51] S. J. Perlmutter et al., *Astrophys. J.* **517**, 565 (1999).

- [52] S. M. Carroll, Living Rev. Relativ. **4**, 1 (2001).
- [53] S. M. Carroll, Phys. Rev. Lett. **81**, 3067 (1998).
- [54] C. Armendariz-Picon, V. Mukhanov, P. J. Steinhardt, Phys. Rev. Lett. **85**, 4438 (2000).
- [55] S. Hellerman, N. Kaloper, L. Susskind, J. High Energy Phys. **06**, 003 (2001).
- [56] T. Padmanabhan, Phys. Rev. D **66**, 021301 (2002).
- [57] R. R. Caldwell, Phys. Lett. B 545, **23** (2002).
- [58] M. Gasperini, M. Piassa, G. Veneziano, Phys. Rev. D **65**, 023508 (2002).
- [59] J. Khoury, A. Weltman, Phys. Rev. Lett. **93**, 171104 (2004).
- [60] E. J. Copeland, M. Sami, S. Tsujikawa, Int. J. Mod. Phys. D **15**, 1753 (2006).
- [61] V. V. Kiselev, Class. Quantum Grav. **20**, 1187 (2003).
- [62] S. Chen, J. Jing, Class. Quantum Grav. **22**, 4651 (2005).
- [63] Y. Zhang, Y. X. Gui, Class. Quantum Grav. **23**, 6141 (2006).
- [64] S. Chen, B. Wang, R. Su, Phys. Rev. D **77**, 124011 (2008).
- [65] Y. H. Wei, Z. H. Chu, Chinese Phys. Lett. **28**, 100403 (2011).
- [66] B. B. Thomas, M. Saleh, T. C. Kofane, Gen. Relativ. Gravit. **44**, 2181 (2012).
- [67] S. Fernando, Mod. Phys. Lett. A **28** 1350189 (2013).
- [68] S. G. Ghosh, Eur. Phys. J. C **76**, 222 (2016).
- [69] Z. Xu, J. Wang, Phys. Rev. D **95**, 064015 (2017).
- [70] M. S. Ma, R. Zhao, Y. Q. Ma, Gen. Relativ. Gravit. **49**, 79 (2017).
- [71] K. Ghaderi, B. Malakolkalami, Grav. Cosmol. **24**, 61 (2018).
- [72] J. de Oliveira, R. D. B. Fontana, Phys. Rev. D **98**, 044005 (2018).
- [73] W. Xu, Y. Wu, EPL **121**, 40001 (2018).
- [74] Md. Shahjalal, Nucl. Phys. B **940**, 63 (2019).
- [75] F. Liu, L. C. Zhang, Chinese J. Phys. **57**, 53 (2019).
- [76] K. Nozari, M. Hajebrahimi, S. Saghafi, Eur. Phys. J. C **80**, 1208 (2020).
- [77] A. Haldar, R. Biswas, Gen. Relativ. Gravit. **52**, 19 (2020).
- [78] B. C. Lütüoğlu, B. Hamil, L. Dahbi, Eur. Phys. J. Plus **136**, 976 (2021).
- [79] R. Ndongmo, S. Mahamat, T. Bouetou Bouetou, T. Crepin Kofane, Phys. Scr. **96**, 095001 (2021)
- [80] K. Nozari, M. Hajebrahimi, Int. J. Geom. Methods Mod. Phys. **19**, 2250177 (2022).

- [81] H. Chen, B. C. Lütfüoğlu, H. Hassanabadi, Z. -W. Long, Phys. Lett. B **827**, 136994 (2022).
- [82] B. Hamil, B. C. Lütfüoğlu, Eur. Phys. J. Plus **137**, 1124 (2022).
- [83] B. P. Singh, Ann. Phys. **441**, 168892 (2022).
- [84] Y. Zhang, Y. B. Ma, Y. Z. Du, H. F. Li, L. C. Zhang, Eur. Phys. J. C **82**, 770 (2022).
- [85] B. Hamil, B. C. Lütfüoğlu, Nucl. Phys. B **990**, 116191 (2023).
- [86] R. Wang, F. Gao, H. Chen, Phys. Dark Universe **40**, 101189 (2023).
- [87] B. Hamil, B. C. Lütfüoğlu, Phys. Dark Universe **42**, 101293 (2023).
- [88] S. Hui, B. Mu, P. Wang, Phys. Dark Universe **43**, 101396 (2024).
- [89] B. Hamil, B. C. Lütfüoğlu, Phys. Dark Universe **44**, 101484 (2024).
- [90] K. Akiyama et al Event Horizon Telescope Collaboration et al, Astrophys. J. Lett. **875**, L1 (2019).
- [91] K. Akiyama et al Event Horizon Telescope Collaboration et al, Astrophys. J. Lett. **875**, L5 (2019).
- [92] K. Akiyama et al Event Horizon Telescope Collaboration et al, Astrophys. J. Lett. **875**, L6 (2019).
- [93] K. Akiyama et al Event Horizon Telescope Collaboration et al Astrophys. J. Lett. **930**, L12 (2022).
- [94] K. Akiyama et al Event Horizon Telescope Collaboration et al Astrophys. J. Lett. **930**, L17 (2022).
- [95] J. L. Synge, Mod. Not. R. Astron. Soc. **131**, 463 (1966).
- [96] J. P. Luminet, Astron. Astrophys. **75**, 228 (1979).
- [97] J. M. Bardeen, *in Black Holes*, ed. by C. Dewitt, B. S. Dewitt (Gordon and Breach, New York), 215-239 (1973).
- [98] R. Shaikh, Phys. Rev. D **100**, 024028 (2019).
- [99] R. A. Konoplya, Phys. Lett. B **795**, 1 (2019).
- [100] S. W. Wei, Y. C. Zou, Y. X. Liu, R. B. Mann, JCAP **08**, 030 (2019).
- [101] C. Bambi, K. Freese, S. Vagnozzi, L. Visinelli, Phys. Rev. D **100**, 044057 (2019).
- [102] S. Vagnozzi, L. Visinelli, Phys. Rev. D **100**, 024020 (2019).
- [103] A. Allahyari, M. Khodadi, S. Vagnozzi, D. F. Mota, JCAP **02**, 003 (2020).
- [104] M. Khodadi, A. Allahyari, S. Vagnozzi, D. F. Mota, JCAP **09**, 026 (2020).
- [105] G. Z. Babar, A. Z. Babar, F. Atamurotov, Eur. Phys. J. C **80**, 761 (2020).
- [106] R. Kumar, S. G. Ghosh, Astrophys. J. **892**, 78 (2020).
- [107] M. Zhang, M. Guo, Eur. Phys. J. C **80**, 790 (2020).
- [108] P. C. Li, M. Guo, B. Chen, Phys. Rev. D **101**, 084041 (2020).
- [109] M. Ghasemi-Nodehi, M. Azreg-Aïnou, K. Jusufi, M. Jamil, Phys. Rev. D **102**, 104032 (2020).

- [110] F. Atamuratov, K. Jusufi, M. Jamil, A. Abdujabbarov, M. Azreg-Ainou, *Phys. Rev. D* **104**, 064053 (2021).
- [111] M. Zhang, J. Jiang, *Phys. Rev. D* **103**, 025005 (2021).
- [112] T. Bronzwaer, H. Falcke, *Astrophys. J.* **920**, 155 (2021).
- [113] J. Peng, M. Guo, X. H. Feng, *Chinese Phys. C* **45**, 085103 (2021).
- [114] A. Chowdhuri, A. Bhattacharyya, *Phys. Rev. D* **104**, 064039 (2021).
- [115] J. Rayimbaev, B. Majeed, M. Jamil, K. Jusufi, A. Wang, *Phys. Dark Universe* **35**, 100930 (2022).
- [116] B. P. Singh, *Ann. Phys.* **441**, 168892 (2022).
- [117] R. Roy, S. Vagnozzi, L. Visinelli, *Phys. Rev. D* **105**, 083002 (2022).
- [118] Y. Chen, R. Roy, S. Vagnozzi, L. Visinelli, *Phys. Rev. D* **106**, 043021 (2022).
- [119] R. C. Pantig, L. Mastrototaro, G. Lambiase, A. Övgün, *Eur. Phys. J. C* **82**, 1155 (2022).
- [120] K. S. Virbhadra, *Phys. Rev. D* **106**, 064038 (2022).
- [121] S. L. Adler, K. S. Virbhadra, *Gen. Relativ. Gravit.* **54**, 93 (2022).
- [122] Y. -Z. Du, H. -F. Li, X. -N Zhou, W. -Q. Guo, R. Zhao, *Chinese Phys. C* **46**, 122002 (2022).
- [123] A. Das, A. Saha, S. Gangopadhyay, *Class. Quantum Grav.* **40**, 015008 (2023).
- [124] W. D. Guo, S. W. Wei, Y. X. Liu, *Eur. Phys. J. C* **83**, 197 (2023).
- [125] A. Uniyal, S. Kanzi, I. Sakalli, *Eur. Phys. J. C* **83**, 668 (2023).
- [126] A. Övgün, R. C. Pantig, A. Rincón, *Eur. Phys. J. Plus* **138**, 192 (2023).
- [127] N. U. Molla, U. Debnath, *Ann. Phys.* **453**, 169304 (2023).
- [128] G. J. Olmo, J. L. Rosa, D. Rubiera-Garcia, D. Sáez-Chillón Gómez, *Class. Quantum Grav.* **40**, 174002 (2023).
- [129] B. Hamil, B. C. Lütfüoğlu, L. Dahbi, arXiv:2307.16287 [gr-qc].
- [130] D. P. Theodosopoulos, T. Karakasis, G. Koutsoumbas, E. Papantonopoulos, arXiv:2311.02740 [gr-qc].
- [131] F. Atamuratov, M. Jamil, K. Jusufi, *Chinese Phys. C* **47**, 035106 (2023).
- [132] B. Hamil, B. C. Lütfüoğlu, *Chinese Phys. C* **48**, 055102 (2024).
- [133] H. Hoshimov, O. Yunusov, F. Atamurotov, M. Jamil, A. Abdujabbarov, *Phys. Dark Universe* **43**, 101392 (2024).
- [134] B. P. Abbott et al. [LIGO Scientific and Virgo Collaborations], *Phys. Rev. Lett.* **116**, 061102 (2016).
- [135] B. P. Abbott et al. [LIGO Scientific and Virgo Collaborations], *Phys. Rev. Lett.* **119**, 161101 (2017).

- [136] W. H. Press, ApJ **170**, L105 (1971).
- [137] R. A. Konoplya, Gen. Relativ. Gravit. **34**, 329 (2002).
- [138] R. A. Konoplya, A. Zhidenko, Rev. Mod. Phys. **83**, 793 (2011).
- [139] R. A. Konoplya, Z. Stuchlik, A. Zhidenko, Phys. Rev. D **98**, 104033 (2018).
- [140] Á. Rincón, G. Panotopoulos, Phys. Rev. D **97**, 024027 (2018).
- [141] C. Chirenti, Braz. J. Phys. **48**, 102 (2018).
- [142] O. J. Tattersall, Phys. Rev. D **98**, 104013 (2018).
- [143] Y. S. Myung, D. -C. Zou, Phys. Lett. B **790**, 400 (2019).
- [144] R. A. Konoplya, A. F. Zinhailo, Z. Stuchlik, Phys. Rev. D **99**, 124042 (2019).
- [145] J. L. Blázquez-Salcedo, S. Kahlen, J. Kunz, Eur. Phys. J. C **79**, 1021 (2019).
- [146] R. A. Konoplya, A. F. Zinhailo, Eur. Phys. J. C **80**, 1049 (2020).
- [147] C. Liu, T. Zhu, Q. Wu, K. Jusufi et al, Phys. Rev. D **101**, 084001 (2020).
- [148] K. Jusufi, Phys. Rev. D **101**, 084055 (2020).
- [149] R. A. Konoplya, Phys. Lett. B **804**, 135363 (2020).
- [150] S. H. Hendi, A. Nemati, K. Lin, M. Jamil, Eur. Phys. J. C **80**, 296 (2020).
- [151] S. H. Hendi, S. Hajkhalili, M. Jamil, M. Momennia, Eur. Phys. J. C **81**, 1112 (2021).
- [152] S. Kanzi, I. Sakalli, Eur. Phys. J. C **81**, 501 (2021).
- [153] M. A. Anacleto, F. A. Brito, J. A. V. Campos, E. Passos, Ann. Phys. **434**, 168662 (2021).
- [154] I. Sakalli, G. Tokgöz Hyusein, Turk. J. Phys. **45**, 43 (2021).
- [155] K. Jafarzade, M. K. Zangeneh, F. S. N. Lobo, JCAP **04**, 008 (2021).
- [156] A. Ghosh, R. Brito, A. Buonanno, Phys. Rev. D **103**, 124041 (2021).
- [157] M. Okyay, A. Övgün, JCAP **01**, 009 (2022).
- [158] R. C. Pantig, L. Mastrototaro, G. Lambiase, A. Övgün, Eur. Phys. J. C **82**, 1155 (2022).
- [159] H. Chen, H. Hassanabadi, B. C. Lütfüoğlu, Z. W. Long, Gen. Relativ. Gravit. **54**, 143 (2022).
- [160] I. Sakalli, S. Kanzi, Turk. J. Phys. **46**, 1 (2022).
- [161] R. A. Konoplya, Phys. Rev. D **107**, 064039 (2023).
- [162] N. Heidari, H. Hassanabadi, Phys. Lett. B **839**, 137814 (2023).
- [163] M. A. Anacleto, F. A. Brito, J. A. V. Campos, E. Passos, Eur. Phys. J. C **83**, 298 (2023).
- [164] S. K. Jha, Eur. Phys. J. C **83**, 952 (2023).

- [165] G. Lambiase, R. C. Pantig, D. J. Gogoi, A. Övgün, *Eur. Phys. J. C* **83**, 679 (2023).
- [166] D. J. Gogoi, A. Övgün, D. Demir, *Phys. Dark Universe* **62**, 101314 (2023).
- [167] A. Al-Badawi, A. Kraishan, *Chinese J. Phys.* **87**, 59 (2024).
- [168] C. H. Nam, *Gen. Relativ. Gravit.* **53**, 1 (2020).
- [169] S. G. Ghosh, S. D. Maharaj, D. Baboolal, T. H. Lee, *Eur. Phys. J. C* **78**, 90 (2018).
- [170] R. B. Ndongmo, S. Mahamat, C. B. Tabi, T. B. Bouetou, T. C. Kofane, *Phys. Dark Universe* **42**, 101299 (2023).
- [171] S. W. Hawking, *Commun. Math. Phys.* **43**, 199 (1975).
- [172] B. P. Singh, S. G. Ghosh, *Ann. Phys.* **395**, 127 (2018).
- [173] S. W. Hawking, D. N. Page, *Commun. Math. Phys.* **87**, 577 (1983).
- [174] R. Moderski, M. Rogatko, *Phys. Rev. D* **64**, 044024 (2001).
- [175] H. T. Cho, *Phys. Rev. D* **68**, 024003 (2003).
- [176] J. Jing, *Phys. Rev. D* **69**, 084009 (2004).
- [177] C. -Y. Chen, P. Chen, *Phys. Rev. D* **99**, 104003 (2019).
- [178] M. Bouhmadi-Lopez, S. Brahma, C. -Y. Chen, P. Chen, D. Yeom, *J. Cosmol. Astropart. Phys.* **07**, 066 (2020).
- [179] N. Herceg, T. Jurić, A. Samsarov, I. Smolić, K. S. Gupta, arxiv:2310.06018 [hep-th].
- [180] B. Carter, *Phys. Rev.* **174**, 1559 (1968).
- [181] B. F. Schutz, C. M. Will, *Astrophys. J.* **291**, 33 (1985).
- [182] B. Mashhoon, *Phys. Rev. D* **31**, 290 (1985).
- [183] S. Iyer, C. M. Will, *Phys. Rev. D* **35**, 3621 (1987).
- [184] J. Matyjasek, M. Opala, *Phys. Rev. D* **96**, 024011 (2017).
- [185] R. Konoplya, A. Zhidenko, A. Zinhailo, *Class. Quant. Grav.* **36**, 155002 (2019).
- [186] V. Ferrari, B. Mashhoon, *Phys. Rev. D* **30**, 295 (1984).